Nano Research 2017, 10(2): 626–642
DOI 10.1007/s12274-016-1322-4
Research Article
ISSN 1998-0124
CN 11-5974/O4

Magnetic iron oxide nanoparticles accelerate osteogenic differentiation of mesenchymal stem cells via modulation of long noncoding RNA *INZEB2*

Qiwei Wang[1,2], Bo Chen[1,2], Fang Ma[3], Shikang Lin[4], Meng Cao[2], Yan Li[1], and Ning Gu[1,2] (✉)

[1] *State Key Laboratory of Bioelectronics, Jiangsu Key Laboratory for Biomaterials and Devices, School of Biological Sciences & Medical Engineering, Southeast University, Nanjing 210096, China*
[2] *Collaborative Innovation Center of Suzhou Nano Science and Technology, Suzhou 215123, China*
[3] *Key Laboratory of Developmental Genes and Human Diseases in Ministry of Education, Institute of Life Sciences, Southeast University, Nanjing 210096, China*
[4] *Signalway Antibody LLC, College Park, MD 20740, USA*

Received: 21 August 2016
Revised: 19 September 2016
Accepted: 30 September 2016

KEYWORDS
iron oxide nanoparticle, mesenchymal stem cell, osteogenic differentiation, long noncoding RNA, magnetogenetics, nano-magnetic bioeffects

ABSTRACT

Nanomaterials are increasingly used for biomedical applications; thus, it is important to understand their biological effects. Previous studies suggested that magnetic iron oxide nanoparticles (IONPs) have tissue-repairing effects. In the present study, we explored cellular effects of IONPs in mesenchymal stem cells (MSCs) and identified the underlying molecular mechanisms. The results showed that our as-prepared IONPs were structurally stable in MSCs and promoted osteogenic differentiation of MSCs as whole particles. Moreover, at the molecular level, we compared the gene expression of MSCs with or without IONP exposure and showed that IONPs upregulated long noncoding RNA *INZEB2*, which is indispensable for maintaining osteogenesis by MSCs. Furthermore, overexpression of *INZEB2* downregulated *ZEB2*, a factor necessary to repress BMP/Smad-dependent osteogenic transcription. We also demonstrated that the essential role of *INZEB2* in osteogenic differentiation was *ZEB2*-dependent. In summary, we elucidated the molecular basis of IONPs' effects on MSCs; these findings may serve as a meaningful theoretical foundation for applications of stem cells to regenerative medicine.

1 Introduction

Advances in nanotechnology and stem cell biology research during the past decades have contributed to the progress of regenerative medicine [1, 2]. Manipulation of stem cell differentiation is an attractive area in the field of development of new nanotechnologies for tissue engineering [3]. Recent studies suggest that

Address correspondence to guning@seu.edu.cn

magnetic iron oxide nanoparticles (IONPs) may be a promising biomaterial for stimulation of the bone regeneration process and for providing transduction of dynamic mechanical stimulation, which is required for bone tissue formation [4]. In past decades, scaffolds made of different biopolymers and magnetic IONPs were prepared to form various nanostructures, for instance, nanofibrous or nanoporous structures that provide both a three-dimensional microenvironment and magnetic micromechanical stimuli for bone regeneration [5–9]. It is well known that osteogenic differentiation of mesenchymal stem cells (MSCs) is one of the basic processes during formation of bone morphology [10]. One study showed that a magnetic-field-induced IONP assembly can promote differentiation of primary mouse bone marrow cells into osteoblasts [11], suggesting that facilitation of cellular osteogenesis may be the underlying mechanism about the bone repair effect of magnetic IONPs. Nonetheless, magnetic IONPs have been commonly used for *in vivo* tracking of MSCs [12–14], and IONPs' effects on the osteogenic differentiation of MSCs are unclear. Another study revealed that IONPs inhibit dexamethasone-induced osteogenic differentiation of MSCs after preincubation [15]. By contrast, our most recent study showed that *in vitro* treatment with IONPs can promote osteogenic differentiation of MSCs [16]. The inconsistent effects of IONPs on MSC differentiation are partially due to the distinct physicochemical properties of these particles [17]. Therefore, further research is needed to confirm some of these discrepant results.

In recent years, three levels of evaluation on nano-bio-effects have been gradually introduced including the whole-body level, cellular level, and molecular level [18–21]. *In vivo* or cellular assays have invariably served as the initial steps for assessment for biological effects of nanomaterials. Nonetheless, with these conventional results, we can determine only whether the effects appeared and the magnitude of cytotoxicity [22], yet it is still unknown what already happened on the molecular level before those effects emerged, particularly in terms of the mechanism. Due to advances in sequencing techniques and computational methods, it is now generally accepted that RNA can play multiple roles in addition to the central function in genetic information flow from DNA to protein [23, 24]. Generally, the mammalian genome transcribes the vast majority (~70%–90%) of long noncoding RNAs (lncRNAs), which are defined as RNAs more than 100 nucleotides in length [25]. Unlike microRNAs, lncRNAs can fold into more complex secondary structure and have a greater potential for recognition and binding of either proteins or nucleic acids [26]. In other words, lncRNA functions more extensively at the epigenetic level [27], such as the regulation of genome imprinting, mRNA maturation, and chromatin remodeling [28, 29]. Nonetheless, few studies have been focused on regulatory roles of lncRNA in biological effects of nanomaterials.

The aim of this work was to further evaluate the effects of IONPs on osteogenic differentiation of MSCs and to explore the underlying mechanisms at the lncRNA level. Collectively, the results presented here may provide insights into the influential mechanisms of IONPs' cellular effects at the molecular level and can facilitate the application of IONPs to regenerative medicine.

2 Experimental

2.1 Synthesis of IONPs

The polyglucose sorbitol carboxymethyl-ether (PSC) coat of IONPs was prepared by modification of dextran in our laboratory. IONPs were synthesized by a modified method of the classic chemical coprecipitation using alternating-current magnetic field (ACMF)-induced internal-heat mode. In brief, 200 mg of PSC was dissolved in 10 mL of deionized water in a round-bottom plastic tube immobilized in the ACMF induction coil, then a mixture of 60 mg of $FeCl_3$ and 30 mg of $FeCl_2$ dissolved in 15 mL of deionized water was added in. One gram of 28% (w/v) ammonium hydroxide was added with vigorous mechanical stirring (370 rpm, IKA RW20, Germany), then moderate radio frequency heating (Shuangping SPF-06-II device, 390 kHz, 14 A, China) was carried out immediately to cause ACMF to produce heat. The colloidal mixture was heated to 80 ℃ by regulating magnetic-field intensity, and the temperature was maintained for 1 h. Lastly, the mixture was cooled to room temperature and purified with six cycles of ultrafiltration against deionized water using a membrane with a 100-kDa limit.

2.2 Characterization of IONPs

The core diameter of IONPs was analyzed by transmission electron microscopy (TEM; JEOL/JEM-200CX, Japan). Their ζ-potential and hydrodynamic diameter were quantified by dynamic light scattering (DLS) by means of a ζ-potential laser particle size analyzer (Malvern Zetasizer Nano ZS90, UK). The final concentrations of iron in the aqueous solution were measured by inductively coupled plasma mass spectrometry (ICP-MS) on an Optima 5300DV instrument (PerkinElmer, MA, USA). The hysteresis loop of IONPs was measured by means of a vibrating sample magnetometer (LS 7307-9309, Lakeshore Cryotronic, USA). *In vitro* magnetic resonance imaging (MRI) of IONPs was conducted in a clinical MRI scanner (Verio 3T, Siemens, Germany).

2.3 Cell culture

Primary human bone-derived MSCs (hBMSCs) were purchased from Cyagen Biosciences Inc. (CA, USA) and grown at 37 ℃ (in a humidified incubator with 5% (v/v) of CO_2) in the Dulbecco's modified eagle medium (DMEM, Gibco, BRL, USA) supplemented with 10% (v/v) of fetal bovine serum (FBS, Gibco), antibiotics (100 U/mL streptomycin and 100 U/mL penicillin), and 1% (w/v) glutamine. To maintain self-renewal and multiple-differentiation potentials, the cells were cultured at appropriate confluence (70% to 80%) and harvested by means of a 0.25% (w/v) trypsin ethylene diamine tetra-acetic acid (EDTA) solution. All experiments were performed before the 10th passage.

2.4 ICP-MS analysis of cellular uptake of IONPs

Cells were seeded in a 6-well plate (2×10^5 cells per well) and incubated with IONPs at different final concentrations (25, 50, 100, 200, or 300 μg/mL), then harvested after 12, 24, or 48 h of treatment. After cell counting and ultrasonication, the concentration of iron in cell lysates was determined by ICP-MS according to PerkinElmer's operating procedures.

2.5 TEM examination of cells

Cells were seeded in a 6-well plate (10^6 cells per well) and incubated with IONPs at the iron concentration of 100 μg/mL, then harvested after 12-h treatment. The cells were detached and fixed overnight with 2.5% glutaraldehyde in 1× phosphate buffer solution (PBS, pH 7.4) at 4 ℃. The samples were then postfixed in 1% osmium tetroxide, dehydrated in ethanol, and embedded in epon (Sigma-Aldrich, MO, USA). Ultrathin slices (60 to 80 nm) were stained with uranyl acetate and lead citrate and imaged by TEM (JEOL/JEM-200CX, Japan).

2.6 Confocal microscopy

Cells were treated with indocyanine green-conjugated IONPs (ICG-IONPs) for 24 or 48 days and fixed with 4% (v/v) formaldehyde. Then, the cells were stained using Lyso Tracker Green (LT) (Life Technologies, USA) and 4',6-diamidino-2-phenylindole (DAPI) (KeyGEN, China) according to the manufacturer's instructions. The cells were next examined under a laser scanning confocal microscope (TCS SP8, Leica, Germany).

2.7 The CCK-8 assay

This assay was used to measure cell viability. Cells were seeded in a 96-well plate (10^4 cells per well) and grown overnight, and then incubated with IONPs at different final concentrations (25, 50, 100, 200, or 400 μg/mL). After 6-, 12-, or 24-h incubation, the cells were washed twice with PBS, and then the CCK-8 reagent (KeyGEN, China) was added to each well and incubated with cells for 4 h at 37 ℃. Optical density (OD) of each well at 450 nm (for the soluble dye) and at 650 nm (for viable cells) was measured.

2.8 The lactate dehydrogenase (LDH) assay

Cytotoxicity was measured by the release of LDH. Cells were seeded in a 96-well plate (10^4 cells per well) and grown overnight, then subjected to various conditions. The culture supernatants were harvested, and assayed for LDH activity and total protein by means of an LDH Activity Kit (Beyotime Biotechnology, China) and a BCA Assay Kit (KeyGEN, China), respectively.

2.9 RNA isolation and reverse transcription

Cells were seeded in a 6-well plate (10^5 cells per well)

and grown overnight, and incubated with IONPs (final concentration 100 μg/mL) for 7 days. Fresh medium was changed every two days, then harvested with trypsin-EDTA. Total RNA was isolated from the cells using TRIzol (Invitrogen, USA). The purity and concentration of RNA were evaluated by means of the OD_{260}/OD_{280} ratio by micro volume spectroscopy (Nano Photometer, NP80, Implen, Germany). cDNA synthesis was performed in a 25-μL reaction containing 1.25 μg of total RNA, 0.5 mM primers, 50 mM Tris-HCl (pH 8.3), 75 mM KCl, 3 mM $MgCl_2$, 10 mM dithiothreitol (DTT), 20 U of a ribonuclease inhibitor, and 100 U of reverse transcriptase (Takara, China). Next, reverse procedure: 5 min at 25 °C, followed by 60 min at 42 °C, and then inactivation at 70 °C for 15 min.

2.10 Microarray analysis

For lncRNA expression profiling by microarray analysis, 1 μg of cDNA was labeled with Cy5-dCTP (red) or Cy3-dCTP (green) and purified, then hybridized to an Agilent Human lncRNA version 2.0 microarray containing 39303 specific lncRNA probes and 32205 coding transcript probes. Both the IONP-treated group and negative-control group were analyzed in triplicate; therefore, six microarray analyses were performed. After hybridization, the microarrays were washed several times, next scanned and imaged on an Agilent array scanner (G2565CA), then Agilent Feature Extraction software (version 10.7) was used to extract the data. Data normalization of the two channel ratios was achieved using an intensity-dependent ''Lowess'' module implemented in the R language package. Differential expression analysis was conducted in the Agilent GeneSpring software, and the data were extracted and filtered as up- or down-regulated genes according to twofold changes; the Cluster 3.0 software was used for the cluster analysis.

2.11 Bioinformatics analysis

Differentially expressed lncRNAs were subjected to BLAST searches in the known lncRNA Databases (imsRNA, RefSeq, UCSC, ENSEMBL, lncRNAdb, UCRs, H-InvDB, and Hox-ncRNAs) according to their probe sequences. Gene function annotations were analyzed by gene ontology biological processes (http://www.geneontology.org).

2.12 Quantitative polymerase chain reaction (Q-PCR)

The relative expression levels of each gene were determined by Q-PCR; all reactions were conducted in triplicate in a 20-μL reaction mixture containing cDNA, primers, and the SYBR-Green Mix (Takara, China). PCR was run on an ABI Step one plus Q-PCR system under the following conditions: a 10-min denaturation step at 95 °C followed by 40 cycles of 15 s at 95 °C and 60 s at 60 °C. The information on gene-specific primers is shown in Table S1 (in the Electronic Supplementary Material (ESM)). The relative quantification of gene expression was performed by the $2^{-\Delta\Delta Ct}$ method.

2.13 The alkaline phosphatase (ALP) assay

Cells were seeded in a 24-well plate (5×10^4 cells per well), then subjected to relevant treatments. The medium was replaced every 2 days. For the ALP assay, the cells were harvested after 7 days and lysed by means of three freeze–thaw cycles; the supernatants were subjected to the ALP assay and total protein quantification by means of an ALP Activity Kit (KeyGEN, China) and a BCA Assay Kit (KeyGEN, China), respectively.

2.14 Alizarin Red S (ARS) staining

Cells were seeded in a 24-well plate (5×10^4 cells per well) and treated as described for the ALP assay. For the ARS assay, the cells were fixed with 4% (v/v) formaldehyde after 21-day treatment, and then stained with 40 mM ARS (pH 4.2) for 30 min at room temperature. After two washes, the cells were examined and imaged by means of a microscope (Axiovert 40, Zeiss, Germany) to determine formation of mineralized matrix nodules.

2.15 RNA silencing experiments

The small interfering RNA (siRNA) sequences are presented in Table S2 (in the ESM). Pairs of complementary oligonucleotides with these sequences were synthesized (Invitrogen, Carlsbad, CA, USA) and cloned into the pshRNA-H1-Luc lenti-vector

(System Biosciences, Mountain View, CA, USA). The pshRNA-H1-Luc lenti-vectors containing the shRNA sequences and the pPACK Packaging Plasmid Mix were co-transfected into 293T producer cells using Lipofectamine™ 2000 (Invitrogen, Carlsbad, CA, USA). Viral supernatants were harvested after 48 h and used for transfection of MSCs. The knockdown efficiency was evaluated by Q-PCR or immunoblot analyses after 48 h of viral transfection.

2.16 Western blotting

Cells were harvested and lysed in the protein extraction buffer, and the supernatants were mixed with loading buffer containing sodium dodecyl sulfate (SDS), DTT, and bromophenol blue. After boiling for 10 min in sample buffer, proteins were separated by SDS-PAGE in a 10% gel and then transferred to a polyvinylidene difluoride (PVDF) membrane (Millipore, MA, USA). The membrane was blocked with 5% (w/v) nonfat powdered milk in Tris-HCl (pH 7.4) buffer solution containing 0.1% (v/v) Tween-20 (TBST) for 1 h at room temperature and probed with a diluted primary antibody at 4 ˚C overnight. After three washes, the membrane was incubated with a diluted horseradish peroxidase (HRP)-conjugated secondary antibody for 1 h at room temperature. The protein level was measured using an enhanced chemiluminescence (ECL) detection system (ChemiDoc XRS+, Bio-Rad, CA, USA) and imaged by means of a CCD camera. Rabbit anti-human RUNX2 (cat. # 41746), OPN (41290), ZEB2 (38682), GAPDH (41549), and HRP-conjugated goat anti-rabbit IgG antibodies (L3012-2) were acquired from Signalway Antibody LLC. (MD, USA). A rabbit anti-human OCN antibody (ab93876) was purchased from Abcam Biotechnology (UK).

2.17 Statistical analysis

This analysis of the data was performed in the SPSS software (version 19.0), and all values were presented as mean ± SD of more than three independent experiments. The results were subjected to one-way analysis of variance (ANOVA) using the Duncan test to analyze the differences between the untreated and treated groups; differences with a p value less than 0.05 were considered significant. The graphs were generated in Origin 8.0.

3 Results and discussion

3.1 Synthesis and characterization of IONPs

To obtain particles with more uniform sizes, shapes, and magnetic properties, we prepared IONPs by the chemical coprecipitation method in the ACMF-induced internal heat mode instead of external-heating mode; the former is more sensitive and reliable for control of the heating temperature [30, 31]. The physicochemical properties of as-prepared IONPs in ACMF heat mode (AC-IONPs) determined in this study are summarized in Table S3 (in the ESM), including average core diameter, hydrodynamic diameters, ζ-potential in the DMEM medium, and the polydispersity index (PDI). The hydrodynamic diameter of particles was measured by DLS, and the mean size was found to be 30.18 nm. Additionally, TEM images revealed that the as-prepared IONPs dispersed light quite uniformly (Fig. 1(a)), and the mean particle size was ~8.2 nm (Fig. 1(b)). The hydrodynamic size of these NPs measured by intensity was larger than the value obtained by TEM, probably because of the extension of the PSC molecular chain and thickness of the hydrated shell.

Magnetic mechanotransduction has been reported to be a pivotal factor in bone tissue formation [4]. In this regard, we compared magnetic properties of AC-IONPs with those of IONPs used in our previous study [16], which were synthesized by external water bath heating (WB-IONPs). Both types of IONPs are superparamagnetic, but the saturation magnetization of AC-IONPs (93 emu/g) is higher than that of WB-IONPs (77 emu/g) (Fig. 1(c)). Moreover, compared to WB-IONPs, AC-IONPs yielded a darker T2 signal at the same concentration according to T2-weighted MRI (Fig. 1(d)). These results indicated that AC-IONPs have better magnetic properties than WB-IONPs do, and the probable reason is that ACMF induces more stable heat, and consequently the crystal structure of the γ-Fe_2O_3 core and uniformity of particles were better. Hence, AC-IONPs were used in the subsequent experiments instead of WB-IONPs.

3.2 Cellular uptake and cytotoxicity of IONPs

Cellular uptake is a basic and important process in biomedical applications of nanomaterials [32]. To evaluate the cellular uptake of IONPs, ICP-MS was

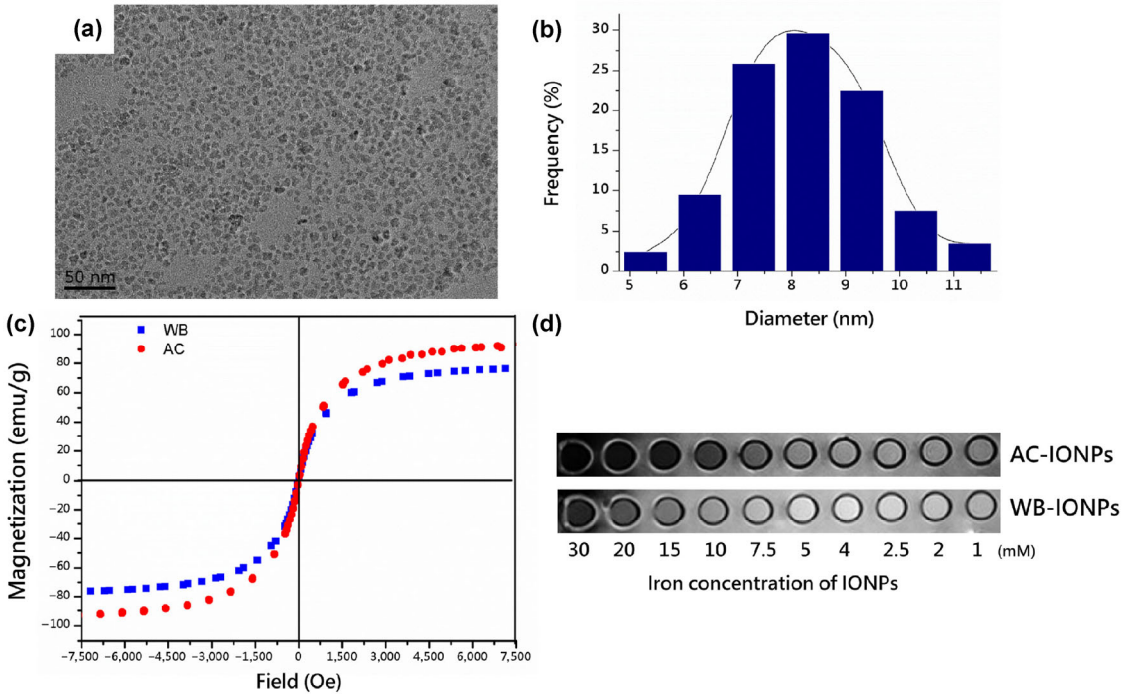

Figure 1 Characterization of the prepared IONPs. (a) A TEM image of as-synthesized IONPs. (b) A size distribution histogram of as-synthesized IONPs, which was obtained by size analysis of >200 particles. (c) The hysteresis loop of IONPs. WB represents IONPs that were synthesized in heat mode in a water bath; AC denotes IONPs that were synthesized in heat mode in an alternating-current (AC) magnetic field. (d) T2-weighted MRI of the prepared IONPs at different concentrations.

used for quantification of iron in cell lysates. As shown in Fig. 2(a), the uptake of IONPs by MSCs was time- and concentration-dependent within the tested range. The concentrations of iron in each cell according to the quantity of cells at each checkpoint were calculated next (Fig. 2(a)). We noticed that there was no significant difference between 24-h and 48-h groups, indicating that the uptake by a single cell was completed within 24 h. To examine the internalization of IONPs more directly, TEM was employed. The results revealed that IONPs were taken up by cells after 12-h exposure and were located in lysosomes partially (Fig. 2(b)). This result is consistent with data from other studies, where the fate of IONPs in human MSCs was systematically studied by synchrotron radiation-based techniques; it was found that cellular internalized IONPs is quite stable and these particles almost escape lysosomes in their initial chemical form for up to 14 days [33, 34]. We next modified the PSC shell of IONPs with molecular ICG and performed confocal microscopy. We noticed that IONPs were located in lysosomes after 24 h of treatment and largely escaped from lysosomes after 48 h (Fig. 2(c)). According to the above results, our as-prepared IONPs may undergo cellular internalized and be structurally stable in MSCs for at least 48 h.

To evaluate the biocompatibility of IONPs, we performed the cell viability assay to examine acute cytotoxicity. Briefly, cells were incubated with various concentrations of IONPs for 6, 12, or 24 h and then subjected to the CCK-8 assay to determine cell viability. The results showed that IONPs had little or no toxic effect on MSCs in a time- and dose-dependent manner: The cells retained viability of more than 90% at all the tested doses and time points (Fig. 2(d)). After 24 h of exposure, the viability decreased by 7.45% and 8.65% at iron concentrations 200 and 400 μg/mL, respectively. We also quantified the LDH release from MSCs treated with various IONPs at 100 μg/mL (including Fe_2O_3@PSC-AC, Fe_2O_3@PSC-WB, or Fe_2O_3 coated by dimercaptosuccinic acid, Fe_2O_3@ DMSA) for 2, 7, 14, and 21 days (Fig. 2(e)). Both types of PSC-coated IONPs caused LDH leakage of less than 9%, whereas DMSA-coated IONPs exerted greater long-term cytotoxicity,

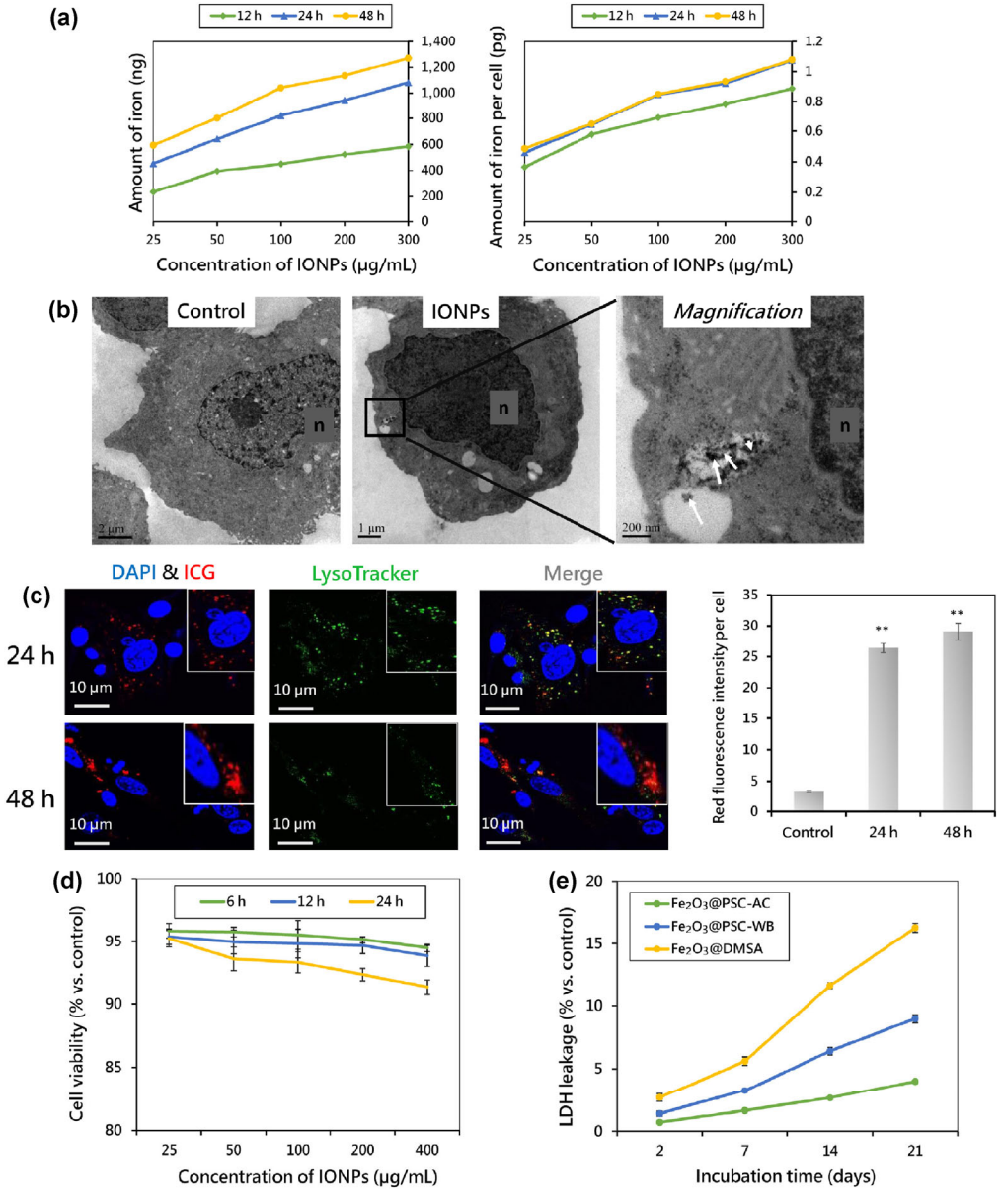

Figure 2 Cellular uptake and cytotoxicity of the prepared IONPs. (a) Total amounts of iron in the cells treated with different concentrations of IONPs for 12, 24, or 48 h, as measured by ICP-MS. Amounts of iron in each cell were calculated from the number of cells at each checkpoint. (b) TEM images of MSCs with IONP treatment (100 μg/mL for 12 h) or without. A higher-magnification image of the indicated portion is shown in the right panel. (c) Laser confocal images of MSCs with ICG-IONP treatment for 24 or 48 h. Red: ICG-IONPs, green: lysosome, blue: nucleus. Red fluorescence intensity in each cell was evaluated in the ImageJ software. Scale bar: 10 μm. (d) Cell viability was measured by the CCK-8 assay after 6, 12, or 24 h of treatment with IONPs at various concentrations. (e) The quantitative lactate dehydrogenase (LDH) leakage assay revealed cytotoxicity induced by Fe_2O_3@PSC-AC, Fe_2O_3@PSC-WB, and Fe_2O_3@DMSA at various timepoints. All bars represent mean ± SD, $n = 3$, $^{**}p < 0.01$.

probably due to the differences in encapsulating materials. Moreover, Fe_2O_3@PSC-AC had better crystal structure than Fe_2O_3@PSC-WB did [30]; thus, less leaching of free iron was taking place, which resulted in lesser LDH leakage after 7 days.

3.3 Global gene expression changes in IONP-treated MSCs

We next performed a genome-wide analysis to analyze changes in global gene expression in IONP-treated

MSCs. According to filtering criteria, the genes whose expression levels changed at least twofold were considered differentially expressed; this approach revealed that 3,723 protein-coding and 1,016 noncoding RNAs (Fig. 3(a)) were affected by IONP exposure. For validation of the microarray results, we randomly selected several candidate lncRNAs and performed quantitative analysis by Q-PCR. After IONP treatment for 7 days, expression levels of *RNA42162*, *RNA9674*, *RNA23048*, *RNA12847*, and *RNA36488* remarkably increased, while expression levels of *RNA5772* and *RNA144089* decreased significantly as compared with the untreated group (Fig. 3(b)). In addition, these aberrations were dependent on the concentration of IONPs during the treatment (Fig. 3(b)). Furthermore, the correlation between expression levels of lncRNAs detected by microarray analysis and Q-PCR was evaluated in this study. We found that the results of the two methods had a significant correlation (Fig. 3(c)), which suggested that Q-PCR may be used instead of microarray analysis for assessment of expression of specific lncRNAs.

3.4 Functional analyses of IONP-affected genes in MSCs

To obtain an overview of the biological processes and molecular functions that are potentially regulated by IONPs in MSCs, Gene Ontology (GO) analysis was conducted to acquire defined annotations that represent gene properties [35, 36]. IONP-affected proteins broadly represented diverse biological processes and molecular functions, and the affected GO terms (which correlated with osteogenic differentiation) could mainly be classified into cellular adhesion, morphology, and signaling (Fig. 4(a)). Both cell–cell adhesion and adhesion to the extracellular matrix can facilitate interactions of receptors, cellular communication, and focal adhesion formation, suggesting that cell adhesion plays a pivotal role in cellular morphology and differentiation [37]. Multiple cell signaling pathways have been reported

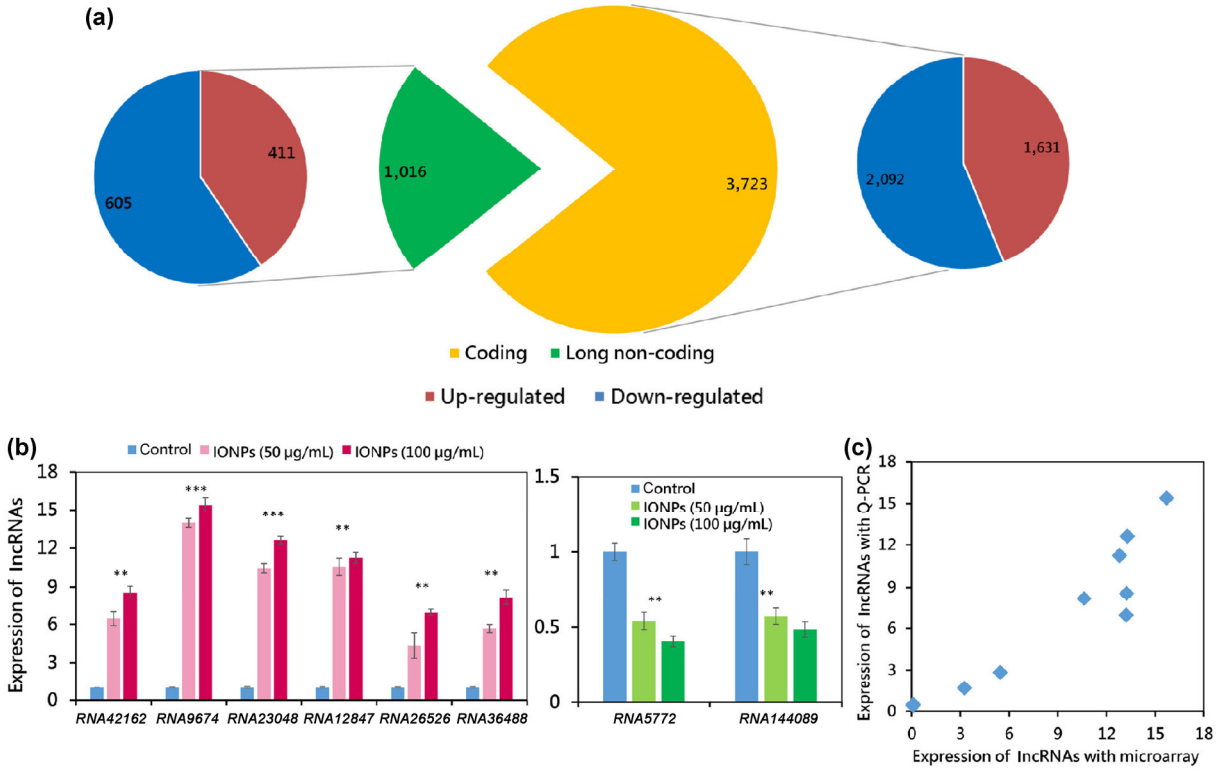

Figure 3 Global gene expression changes in IONP-treated MSCs. (a) Pie chart representation of the number of protein-coding and noncoding RNAs deregulated in IONP-treated MSCs (fold change > 2, $p < 0.05$). (b) Expression levels of lncRNAs measured by Q-PCR after exposure to 50 or 100 μg/mL IONPs for 7 days. Q-PCR results were obtained by the $2^{-\Delta\Delta Ct}$ method. All bars represent mean ± SD, $n = 3$, $^{**}p < 0.01$, $^{***}p < 0.001$. (c) Correlation between expression levels of lncRNAs measured by microarray analysis and Q-PCR.

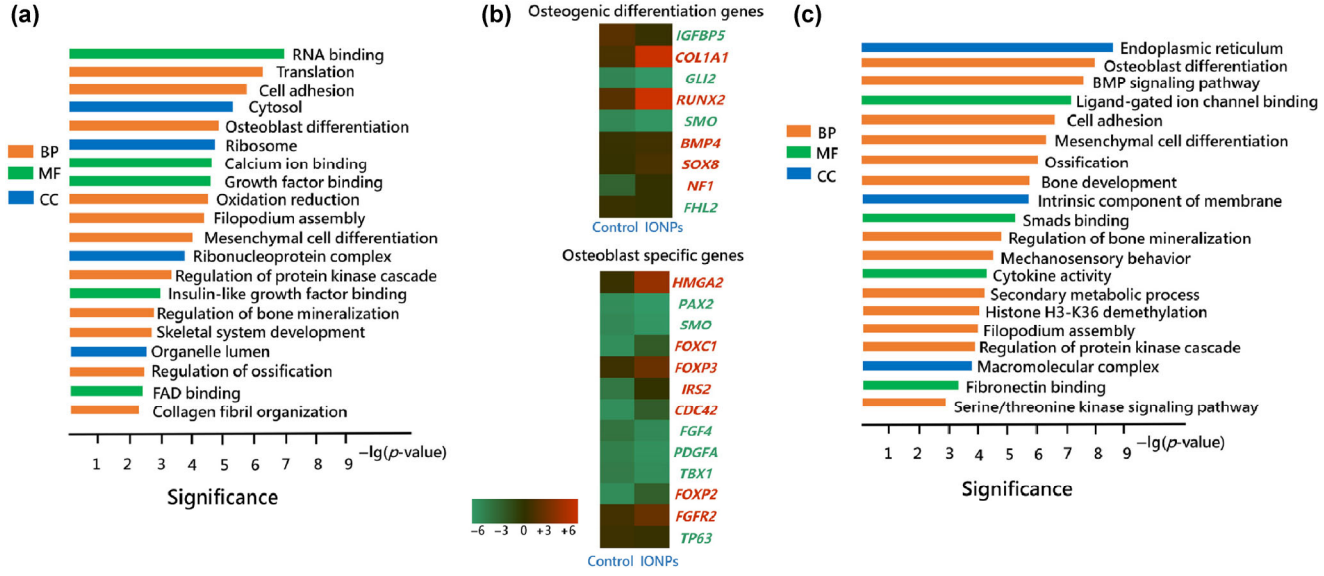

Figure 4 Functional annotation of differentially expressed genes in IONP-treated MSCs. (a) Gene ontology analysis of differentially expressed coding genes. Top 20 significant Gene Ontology terms are listed. BP, biological process; MF, molecular function; CC, cellular component. (b) A heatmap was generated with a partial list of deregulated protein-coding genes involved in osteogenic differentiation and osteoblast-specific genes with the corresponding fold changes according to the color scale on the left. Gene expression clustering was performed in the Cluster 3.0 software and viewed in the TreeView software. (c) Gene ontology analysis of coding genes correlating with the differentially expressed lncRNAs. Top 20 significant Gene Ontology terms are listed.

to participate in osteogenic differentiation [38–41], whose three terms—"calcium ion pathway", "protein kinase pathway", and "insulin-like growth factor receptor pathway"—were enriched in our dataset (Fig. 4(a)). There are several differences in morphology between MSCs and osteoblasts, for example, more filopodia are put out by osteoblasts [42]. Collagen fibrils are a major component of the extracellular bone matrix secreted by osteoblasts and accumulates in the mineralized bone coupled with calcium phosphate [43]. Our results indicated that GO terms including cell morphology, collagen fibril organization, and cell differentiation were enriched in this dataset (Fig. 4(a)). Furthermore, protein-coding genes involved in GO terms "osteogenic differentiation" and "osteoblast-specific genes" were also present in the list (Fig. 4(b)).

It is well established that lncRNAs function by influencing their associated genes. In addition, to obtain more comprehensive information about lncRNA regulation of the IONP-driven osteogenic differentiation of MSCs, we calculated the Pearson correlation coefficient (PCC) between differentially expressed lncRNAs and mRNAs, and significantly coexpressed lncRNA–mRNA pairs are presented in Table S4 (in the ESM). Hence, to determine possible involvement of lncRNAs in the regulation of IONPs' biological effects on MSCs, we applied GO analysis to code genes that were significantly coexpressed with lncRNAs. According to the results, a greater number of enriched GO terms that are closely related to osteogenesis was obtained, including the BMP signaling pathway, Smad binding, and mechanosensory behavior (Fig. 4(c)). The BMP/Smad signaling cascade is the canonical signaling pathway that facilitates osteogenic differentiation of MSCs [44]. In particular, BMPs mediate both phosphorylation and nuclear translocation of Smads, which promote transcription of osteogenesis-associated genes (for example, *RUNX2*) by recruiting specific transcription factors [45]. One study showed that nanoscale mechanical stress can drive MSCs to differentiate into osteoblasts because focal adhesion is activated by stress-mediated cellular force isotropy, thus regulating osteogenic differentiation [46]. Overall, these results revealed not only the potential role of IONPs in osteogenic differentiation of MSCs but also

the possible participation of lncRNAs in the control of this effect.

3.5 Promotion of osteogenic differentiation by whole IONPs

To determine the potential role of IONPs in osteogenic differentiation of MSCs, we examined ALP activity and bone matrix secretion (two popular markers for analysis of osteogenic differentiation at an early or late stage [47]) in IONP-treated MSCs. The ferric ion and molecular PSC are the direct acidolysis products of γ-Fe_2O_3 particles in the lysosome; therefore, we set up control groups treated with the ferric ion and molecular PSC. ALP activity showed an obvious enhancement during exposure to 100 μg/mL IONPs, in agreement with our previous study [16]. Compared with the untreated group, MSCs exposed to Fe^{3+} for 7 or 14 days showed no obvious increase in ALP activity at all the concentrations analyzed (Fig. 5(a)). In contrast, the ALP activity decreased in all the molecular-PSC exposure groups (Fig. 5(b)). Furthermore, MSCs exposed to either 100 μg/mL molecular PSC or 100 μM Fe^{3+} for 21 days secreted negligible amounts of mineralized nodules as compared with exposure to IONPs or osteogenesis-inducing supplements (OS) (Fig. 5(c)). In accordance with the above results, we concluded that the osteogenic differentiation effect was promoted by whole IONPs, rather than by the ferric ion or the PSC molecules. This result is consistent with the above-mentioned finding that cellular internalized IONPs can be considered structurally stable.

3.6 lncRNA *INZEB2* is necessary for IONP-driven osteogenic differentiation

To determine the molecular mechanism of the regulation of IONP-driven osteogenic differentiation by lncRNAs, we quantified the significantly overexpressed lncRNAs according to microarray results during exposure to IONPs for 2, 5, or 7 days. Among these selected lncRNAs, we found that *LOC105373660* was upregulated during IONP exposure, and the expression of this lncRNA reached the same level as that seen in osteoblasts after 7 days of IONP treatment (Fig. 6(a)). Additionally, this overexpression was dose-dependent on the IONP exposure (Fig. 6(b)). By contrast, the expression level showed no significant change when MSCs were treated with OS (Fig. 6(c)),

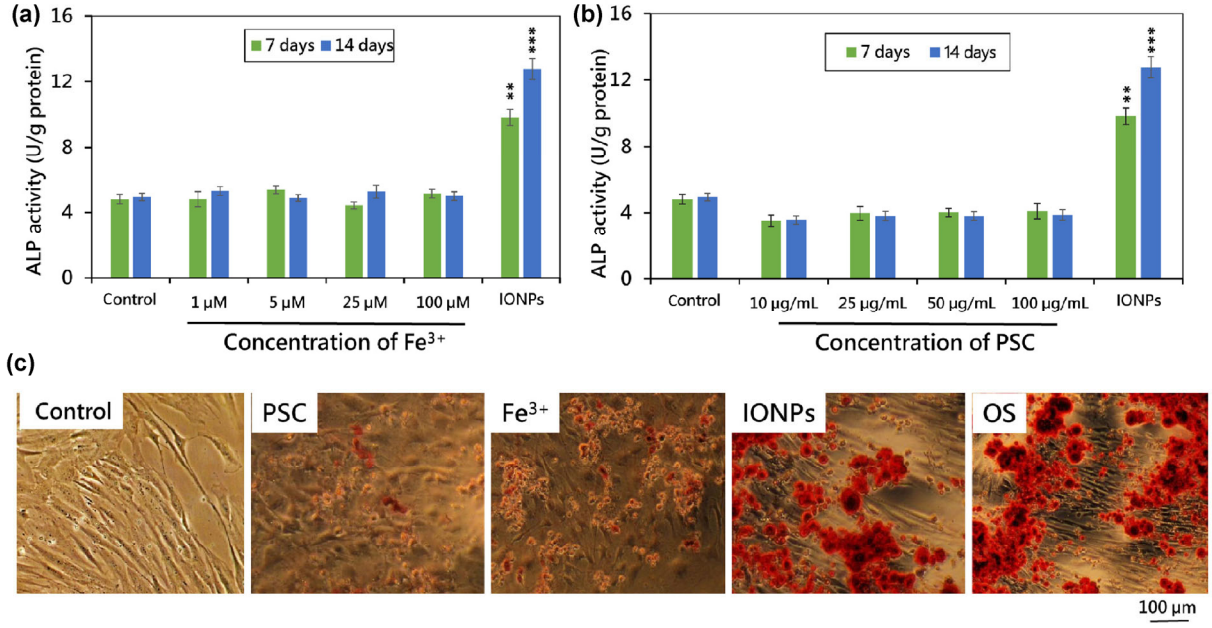

Figure 5 Evaluation of osteogenic differentiation. Effects of different concentrations of Fe^{3+} (a) or molecular PSC (b) on the ALP activity of MSCs. All bars represent mean ± SD, $n = 3$, $^{**}p < 0.01$; $^{***}p < 0.001$. (c) Alizarin Red S staining images. MSCs (the fifth passage) were treated with 100 μM Fe^{3+}, 100 μg/mL molecular PSC, 100 μg/mL IONPs, or OS for 21 days. OS: osteogenesis-inducing supplements, scale bar: 100 μm.

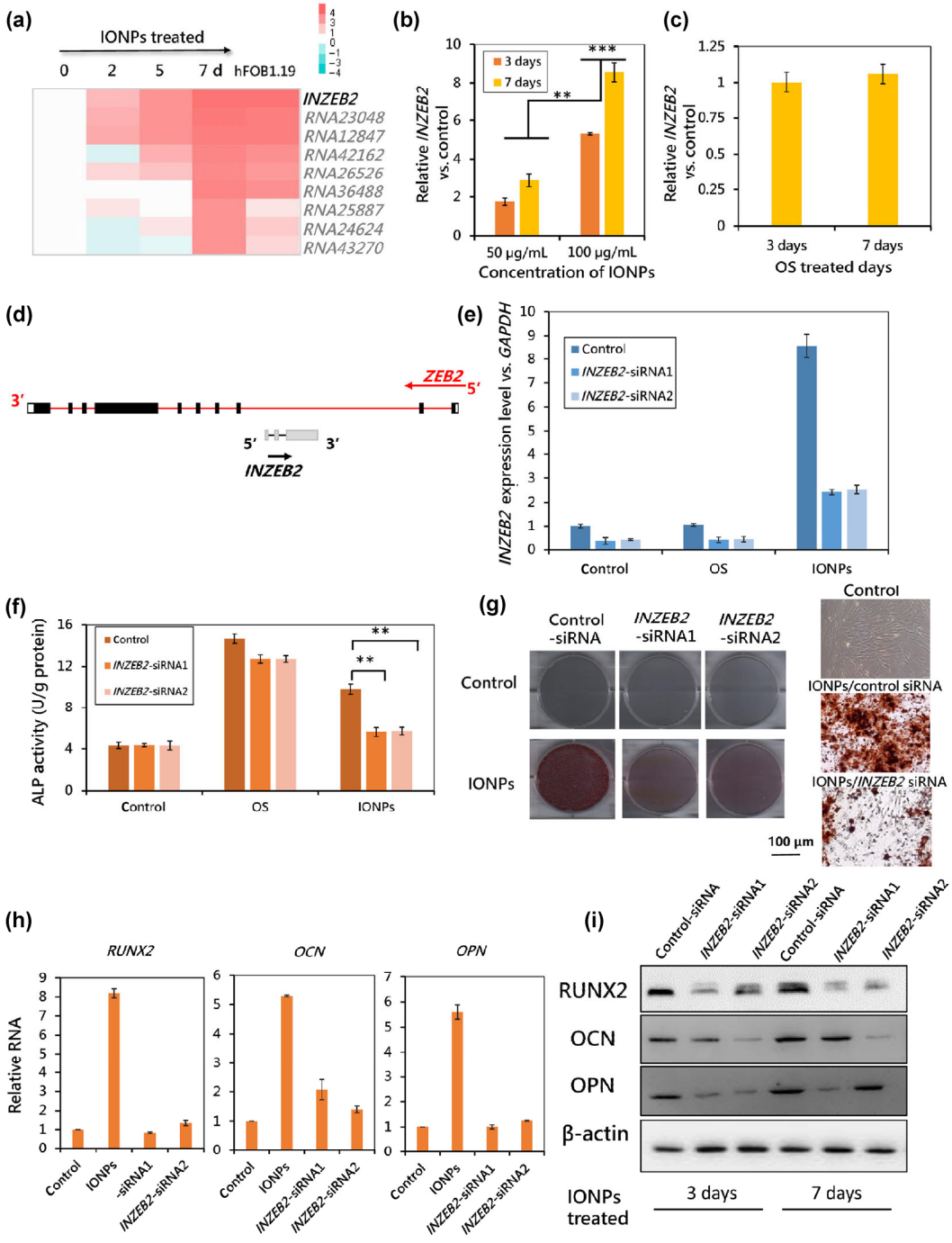

Figure 6 LncRNA *INZEB2* is necessary during IONP-driven osteogenic differentiation. (a) A heatmap was generated with a partial list of deregulated lncRNAs with the corresponding fold changes according to the color scale on the left. Gene expression clustering was performed by means of the Cluster 3.0 software and viewed in software TreeView. (b) Relative expression of *INZEB2* measured by Q-PCR after exposure to 50 or 100 μg/mL IONPs for 3 or 7 days. (c) Relative expression of *INZEB2* measured by Q-PCR after treatment with OS for 3 or 7 days. (d) Genomic context of intron/exon boundaries of *INZEB2* and *ZEB2*. (e) Expression of *INZEB2* measured by Q-PCR after transfection of *INZEB2*-siRNAs. (f) Effects of an *INZEB2* knockdown on the ALP activity of MSCs. (g) Alizarin Red S staining images. Effects of the *INZEB2* knockdown on the mineralized-nodule formation in MSCs. Scale bar: 100 μm. (h) Expression of *RUNX2*, *OCN*, and *OPN* mRNAs measured by Q-PCR after the *INZEB2* knockdown and OS treatment for 3 days. (i) Protein expression of RUNX2, OCN, OPN measured by western blotting after the *INZEB2* knockdown and OS treatment for 3 or 7 days. Q-PCR results were obtained by the $2^{-\Delta\Delta Ct}$ method. All bars represent mean ± SD, $n = 3$, $^{**}p < 0.01$; $^{***}p < 0.001$.

suggesting that overexpression of this lncRNA could not be caused by OS treatment. Using the sequence and genomic location for BLAST searches in the Ensembl Genome Database (www.ensembl.org/), we found that the putative transcript is located in chromosomal region 2*q*22.3 (*Chr* 2: 144,440,543-50,689) and is transcribed from the partial opposite strand of *ZEB2*'s intron 2 (Fig. 6(d)). Therefore, we named it *INZEB2* (intronic *ZEB2*).

To address the relevance of *INZEB2* to the commitment of MSCs to the osteoblastic lineage, we next knocked down *INZEB2* in MSCs (the third passage) using two independent siRNAs administered via a lentivirus. We achieved the knockdown efficiency of ~60%–70% (Fig. 6(e)), while the cell viability was not changed significantly (data not shown). MSCs were then treated with IONPs at 72 h post-transfection, and we analyzed the two above-mentioned markers in *INZEB2* knockdown MSCs. The results revealed that compared with normal cells, IONP-treated cells showed a notable reduction in both ALP activity and secreted mineralized nodules when we knocked down *INZEB2* (Figs. 6(f) and 6(g)). As shown in Fig. 6(f), ALP activity decreased insignificantly in IONP-treated MSCs compared with OS-treated cells: The main reason was the difference in the mechanism of action of these two osteogenesis-inducing conditions. OS induces osteogenic differentiation by activating the dexamethasone-mediated glucocorticoid receptor pathway; thus, the ALP level remained relatively high (Fig. 6(f)) although *INZEB2* was expressed weakly (Fig. 6(e)). In contrast, in IONP-treated cells, the lack of *INZEB2* had a significant influence on osteogenic differentiation (Figs. 6(f) and 6(g)), suggesting that *INZEB2* is necessary during IONP-induced osteogenic differentiation of MSCs.

The expression of a number of bone-related extracellular matrix proteins including osteocalcin (*OCN*), osteopontin (*OPN*), and type I collagen (*COL I*) are considered another major feature of osteoblasts [48, 49]. Meanwhile, recent studies revealed that *RUNX2* performs a key function in determining osteogenic differentiation of MSCs [50, 51]. Therefore, we examined the expression alterations of *OCN*, *OPN*, and *RUNX2* in *INZEB2* knockdown cells after OS treatment. The results suggested that both mRNA and protein levels of these genes were reduced in *INZEB2* knockdown cells after osteogenesis induction (Figs. 6(h) and 6(i)). The data also showed that *INZEB2* was necessary for maintaining the osteogenic phenotype.

3.7 The role of *INZEB2* in modulating IONP-driven osteogenic differentiation is dependent on *ZEB2*

INZEB2 is embedded in the *ZEB2* gene locus, and *ZEB2* plays an inhibitory role in BMP/Smad-mediated osteogenic differentiation [52]. Therefore, we hypothesized that *INZEB2* maintains osteogenic differentiation depending on repression of *ZEB2* expression. For this purpose, we assessed the expression changes of *ZEB2* after IONP treatment. The results showed that both mRNA and protein levels of *ZEB2* were reduced during IONP-driven osteogenic differentiation (Figs. 7(a) and 7(b)), while the knockdown of *INZEB2* reversed the down-regulation of *ZEB2* (Figs. 7(a) and 7(c)). This finding is consistent with our hypothesis that *INZEB2* acts as an inhibitor of *ZEB2* expression. To determine whether *INZEB2* affects osteogenic differentiation by influencing *ZEB2*, we implemented a knockdown of *ZEB2* (Fig. 7(d)). During treatment with IONPs, the inhibition of ALP activity induced by the *INZEB2* knockdown was reversed by the *ZEB2* knockdown (Fig. 7(e)). Furthermore, a mineralized nodule staining assay showed similar results (Fig. 7(f)). Afterwards, the expression levels of osteogenic genes were analyzed. The results suggested that the knockdown of *ZEB2* restored the expression of RUNX2, OPN, and OCN downregulated by the *INZEB2* knockdown (Fig. 7(g)). These results revealed that the essential role of *INZEB2* in osteogenic differentiation is *ZEB2* dependent.

According to the above findings, a scheme was compiled to briefly describe the possible mechanism underlying the osteogenic-differentiation-promoting effects of IONPs (Fig. 8). *ZEB2*, also known as *SIP1* (Smad-interacting protein 1), is a member of the ZEB protein family with two separated clusters of C_2H_2-type zinc fingers [53] and functions as a DNA-binding transcriptional repressor that interacts with BMP-activated Smads [54]. One study has shown that ZEB2 can recruit transcriptional corepressors (CtBP) to Smads and inhibit transcription of Smad-dependent genes (such as *RUNX2*) [55]. *INZEB2*, which functions

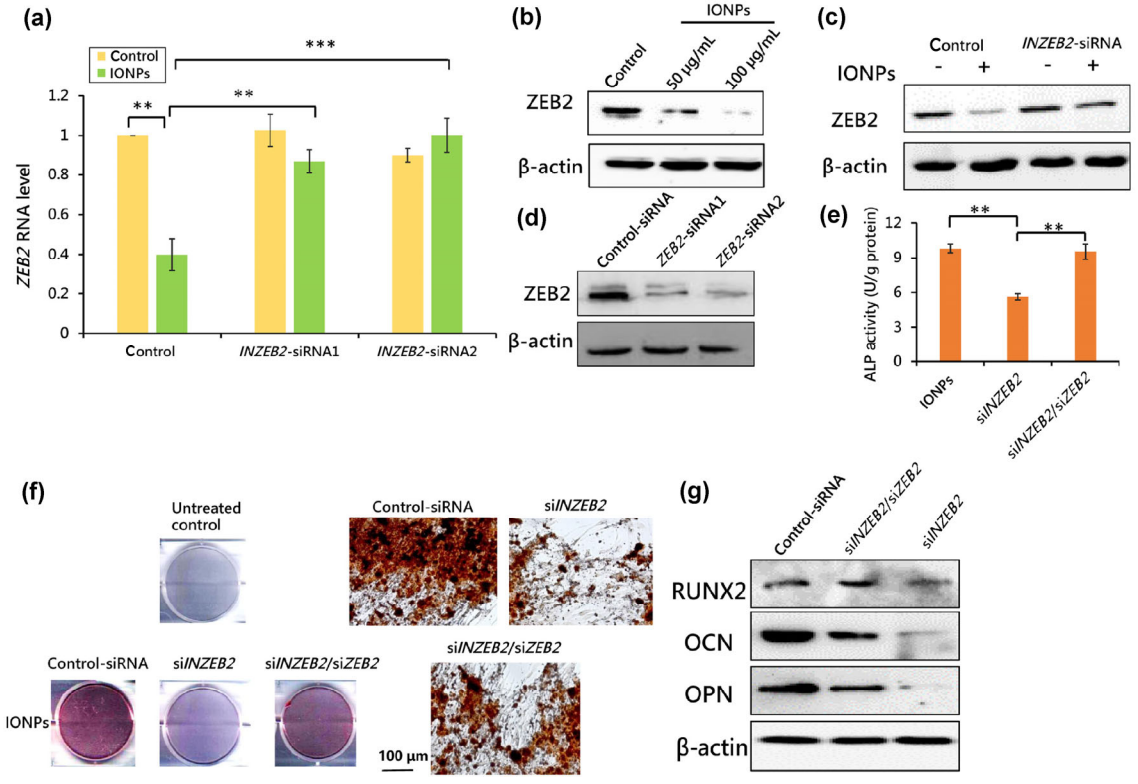

Figure 7 The role of *INZEB2* in the regulation of IONP-driven osteogenic differentiation is *ZEB2* dependent. (a) Relative RNA expression levels *ZEB2* as measured by Q-PCR. (b) Effects on ZEB2 protein levels measured by western blotting after exposure to 50 or 100 μg/mL IONPs. (c) Effects on ZEB2 protein levels measured by western blotting after a knockdown of *INZEB2* in MSCs. (d) Protein expression levels of ZEB2 measured by western blotting after transfection of *ZEB2*-siRNAs. (e) Effects on ALP activity of MSCs after transfection with the indicated siRNA. (f) Alizarin Red S staining images. Effects on the mineralized-nodule formation in MSCs after transfection with the indicated siRNA; the scale bar is 100 μm. (g) Effects on the protein levels measured by western blotting after transfection with the indicated siRNA. Q-PCR results were obtained by the $2^{-\Delta\Delta Ct}$ method. All bars represent mean ± SD, $n = 3$, $^{**}p < 0.01$; $^{***}p < 0.001$.

as a *ZEB2* inhibitor, was upregulated after IONP treatment. Consequently, expression of *ZEB2* was reduced, and Smad-dependent osteogenic gene expression (repressed by *ZEB2)* was reactivated. Accordingly, MSCs were driven to differentiate into osteoblasts.

In this study, our as-prepared IONPs showed lower toxicity toward MSCs (Figs. 2(d) and 2(e)), which was probably due to more stable structure and less free iron [30]. In addition, the main factor of the osteogenic-differentiation-promoting effect was whole IONPs themselves, rather than the iron ion or PSC shell (Fig. 5). The complete structure ensured the effects of IONPs on MSCs. This finding indicated that the magnetic properties of IONPs may contribute to this effect. It is well known that natural intracellular magnetite is responsible for the magnetic perception in animals [56], and cellular internalized IONPs may play an analogous role. The simplest explanation is that IONPs exert torque or pressure on secondary receptors (such as mechanoreceptors) as the particles attempt to align with the geomagnetic field [57]. Alternatively, the rotation of intracellular IONPs might open ion channels directly: For example, cytoskeletal filaments connect the particles to the channels [56]. Opening of these channels allows ions to trigger downstream signaling [58]. Recent studies also suggested that a cytoskeleton reorganization induced by a mechanical force can result in nuclear stretching, and three-dimensional distribution of both chromosomes and transcription factors is altered subsequently [59], and thus downstream signaling events correlating with osteogenic differentiation are also altered [60].

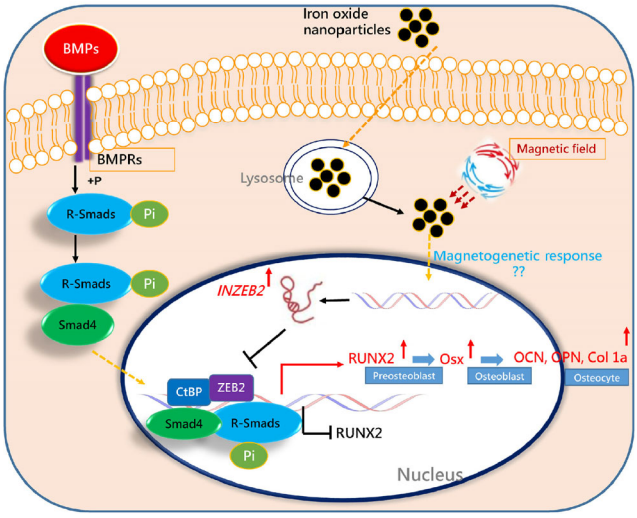

Figure 8 Schematic illustration of the proposed model of IONP-driven osteogenic differentiation of MSCs via *INZEB2* and the BMP/Smad pathway. Under normal conditions, ZEB2 recruits CtBP thus repressing BMPR-activated Smads and inhibiting RUNX2 expression. After treatment with IONPs, *INZEB2* is upregulated and reduces ZEB2 expression; consequently, RUNX2 expression and osteogenic differentiation are unlocked.

To date, there is still a huge knowledge gap regarding IONPs and their possible cellular effects. In other words, we know little about the molecular mechanism behind the interaction between IONPs and cells. One research group studied protein expression changes caused by IONPs with different surface modifications (COOH groups, plain surface, or NH_2 groups) in three human cell lines [61]. On the other hand, organismal complexity correlates with the proportion of the genome transcribed, that is, transcribed into lncRNAs more than protein-coding genes [29], suggesting that the lncRNA-based regulatory mechanism has more diverse functions. Here, we carried out a systematic analysis of lncRNA control over IONP-driven osteogenic differentiation. On the basis of coexpression analysis and functional annotations, the deregulated lncRNAs were found to be involved in many biological processes including the BMP signaling pathway, ligand-gated ion channel binding, cell adhesion, osteoblastic differentiation, Smad binding, and mechanosensory behavior. These results provide a systematic molecular explanation (in terms of lncRNA) for the promotion of osteogenic differentiation by IONPs. Moreover, lncRNA *INZEB2* plays an indispensable role in osteogenic differentiation by repressing Smad-binding protein *ZEB2* and by activating the BMP signaling pathway. Nevertheless, it is still unclear what triggers the overexpression of *INZEB2* and what kinds of mechanisms are involved in the *INZEB2*-driven inhibition of *ZEB2* expression. The mRNA level of *ZEB2* was reduced by IONP exposure (Fig. 7(a)), indicating that *INZEB2* may affect *ZEB2* transcriptionally. Moreover, further studies on how to control these nanomagnetically responsive molecules are necessary and should help to manipulate stem cell fate.

4 Conclusions

Our data support the conclusion that our as-prepared magnetic IONPs promote osteogenic differentiation of MSCs as whole particles, and the IONP-driven magnetogenetic response results in deregulation of numerous genes in our experimental system. Among these genes, lncRNA *INZEB2* is crucial for osteogenic differentiation because it regulates *ZEB2* expression and the BMP/Smads pathway. Our results revealed how IONPs affect osteogenic differentiation of MSCs and how lncRNAs contribute to the regulation of cellular effects of magnetic IONPs. This knowledge should be useful for the development of novel IONP-based approaches to tissue engineering and other biomedical applications.

Acknowledgements

This work was supported by grants from the National Basic Research Program of China (Nos. 2013CB733804 and 2013CB934400), the National Natural Science Foundation of China (NSFC) for Key Project of International Cooperation (No. 61420106012), Special Project on Development of National Key Scientific Instruments and Equipment of China (No. 2011YQ03013403), the Natural Science Foundation of Jiangsu Province (No. BK20130608), the Fundamental Research Funds for the Central Universities and the Graduate Research and Innovation Program of Jiangsu Province in China (No. KYLX15-0167).

Electronic Supplementary Material: Supplementary material (the physicochemical properties of as-prepared IONPs, detailed lncRNA co-expressed mRNA, detailed primers for Q-PCR and siRNA sequences) is available in the online version of this article at http://dx.doi.org/10.1007/s12274-016-1322-4.

References

[1] Wang, F. F.; Zhai, D.; Wu, C. T.; Chang, J. Multifunctional mesoporous bioactive glass/upconversion nanoparticle nanocomposites with strong red emission to monitor drug delivery and stimulate osteogenic differentiation of stem cells. *Nano Res.* **2016**, *9*, 1193–1208.

[2] Weightman, A. P.; Jenkins, S. I.; Chari, D. M. Using a 3-D multicellular simulation of spinal cord injury with live cell imaging to study the neural immune barrier to nanoparticle uptake. *Nano Res.* **2016**, *9*, 2384–2397.

[3] Zhang, S.; Bach-Gansmo, F. L.; Xia, D.; Besenbacher, F.; Birkedal, H.; Dong, M. D. Nanostructure and mechanical properties of the osteocyte lacunar-canalicular network-associated bone matrix revealed by quantitative nanome-chanical mapping. *Nano Res.* **2015**, *8*, 3250–3260.

[4] Henstock, J. R.; Rotherham, M.; Rashidi, H.; Shakesheff, K. M.; El Haj, A. J. Remotely activated mechanotransduction via magnetic nanoparticles promotes mineralization synergistically with bone morphogenetic protein 2: Applications for injectable cell therapy. *Stem Cells Transl. Med.* **2014**, *3*, 1363–1374.

[5] Bock, N.; Riminucci, A.; Dionigi, C.; Russo, A.; Tampieri, A.; Landi, E.; Goranov, V. A.; Marcacci, M.; Dediu, V. A novel route in bone tissue engineering: Magnetic biomimetic scaffolds. *Acta Biomater.* **2010**, *6*, 786–796.

[6] Yun, H. M.; Ahn, S. J.; Park, K. R.; Kim, M. J.; Kim, J. J.; Jin, G. Z.; Kim, H. W.; Kim, E. C. Magnetic nanocomposite scaffolds combined with static magnetic field in the stimulation of osteoblastic differentiation and bone formation. *Biomaterials* **2016**, *85*, 88–98.

[7] Meng, J.; Xiao, B.; Zhang, Y.; Liu, J.; Xue, H. D.; Lei, J.; Kong, H.; Huang, Y. G.; Jin, Z. Y.; Gu, N. et al. Super-paramagnetic responsive nanofibrous scaffolds under static magnetic field enhance osteogenesis for bone repair *in vivo*. *Sci. Rep.* **2013**, *3*, 2655.

[8] Heymer, A.; Haddad, D.; Weber, M.; Gbureck, U.; Jakob, P. M.; Eulert, J.; Noeth, U. Iron oxide labelling of human mesenchymal stem cells in collagen hydrogels for articular cartilage repair. *Biomaterials* **2008**, *29*, 1473–1483.

[9] Dzamukova, M. R.; Naumenko, E. A.; Rozhina, E. V.; Trifonov, A. A.; Fakhrullin, R. F. Cell surface engineering with polyelectrolyte-stabilized magnetic nanoparticles: A facile approach for fabrication of artificial multicellular tissue-mimicking clusters. *Nano Res.* **2015**, *8*, 2515–2532.

[10] Marie, P. J. Targeting integrins to promote bone formation and repair. *Nat. Rev. Endocrinol.* **2013**, *9*, 288–295.

[11] Sun, J. F.; Liu, X.; Huang, J. Q.; Song, L.; Chen, Z. H.; Liu, H. Y.; Li, Y.; Zhang, Y.; Gu, N. Magnetic assembly-mediated enhancement of differentiation of mouse bone marrow cells cultured on magnetic colloidal assemblies. *Sci. Rep.* **2014**, *4*, 5125.

[12] Yang, F.; Li, M. X.; Cui, H. T.; Wang, T. T.; Chen, Z. W.; Song, L.; Gu, Z. X.; Zhang, Y.; Gu, N. Altering the response of intracellular reactive oxygen to magnetic nanoparticles using ultrasound and microbubbles. *Sci. China Mater.* **2015**, *58*, 467–480.

[13] Yang, Z. Z.; Ding, X. G.; Jiang, J. Facile synthesis of magnetic–plasmonic nanocomposites as T_1 MRI contrast enhancing and photothermal therapeutic agents. *Nano Res.* **2016**, *9*, 787–799.

[14] Liu, D.; Yang, F.; Xiong, F.; Gu, N. The smart drug delivery system and its clinical potential. *Theranostics* **2016**, *6*, 1306–1323.

[15] Chen, Y. C.; Hsiao, J. K.; Liu, H. M.; Lai, I. Y.; Yao, M.; Hsu, S. C.; Ko, B. S.; Chen, Y. C.; Yang, C. S.; Huang, D. M. The inhibitory effect of superparamagnetic iron oxide nanoparticle (ferucarbotran) on osteogenic differentiation and its signaling mechanism in human mesenchymal stem cells. *Toxicol. Appl. Pharmacol.* **2010**, *245*, 272–279.

[16] Wang, Q. W.; Chen, B.; Cao, M.; Sun, J. F.; Wu, H.; Zhao, P.; Xing, J.; Yang, Y.; Zhang, X. Q.; Ji, M. et al. Response of MAPK pathway to iron oxide nanoparticles *in vitro* treatment promotes osteogenic differentiation of hBMSCs. *Biomaterials* **2016**, *86*, 11–20.

[17] Assa, F.; Jafarizadeh-Malmiri, H.; Ajamein, H.; Anarjan, N.; Vaghari, H.; Sayyar, Z.; Berenjian, A. A biotechnological perspective on the application of iron oxide nanoparticles. *Nano Res.* **2016**, *9*, 2203–2225.

[18] Williams, D. F. On the mechanisms of biocompatibility. *Biomaterials* **2008**, *29*, 2941–2953.

[19] Klapperich, C. M.; Bertozzi, C. R. Global gene expression of cells attached to a tissue engineering scaffold. *Biomaterials* **2004**, *25*, 5631–5641.

[20] Cheng, K.; Shen, D. L.; Hensley, M. T.; Middleton, R.; Sun, B. M.; Liu, W. X.; De Couto, G.; Marbán, E. Magnetic antibody-linked nanomatchmakers for therapeutic cell targeting. *Nat. Commun.* **2014**, *5*, 4880.

[21] Pan, Y. M.; Wang, L. M.; Kang, S. G.; Lu, Y. Y.; Yang, Z. X.; Huynh, T.; Chen, C. Y.; Zhou, R. H.; Guo, M. Z.; Zhao, Y. L. Gd-metallofullerenol nanomaterial suppresses pancreatic cancer metastasis by inhibiting the interaction of histone deacetylase 1 and metastasis-associated protein 1. *ACS Nano* **2015**, *9*, 6826–6836.

[22] Nair, A. V.; Keliher, E. J.; Core, A. B.; Brown, D.; Weissleder, R. Characterizing the interactions of organic nanoparticles with renal epithelial cells *in vivo*. *ACS Nano* **2015**, *9*, 3641–3653.

[23] Eddy, S. R. Non-coding RNA genes and the modern RNA world. *Nat. Rev. Genet.* **2001**, *2*, 919–929.

[24] Carninci, P.; Kasukawa, T.; Katayama, S.; Gough, J.; Frith, M. C.; Maeda, N.; Oyama, R.; Ravasi, T.; Lenhard, B.; Wells, C. et al. The transcriptional landscape of the mammalian genome. *Science* **2005**, *309*, 1559–1563.

[25] Geisler, S.; Coller, J. RNA in unexpected places: Long non-coding RNA functions in diverse cellular contexts. *Nat. Rev. Mol. Cell Biol.* **2013**, *14*, 699–712.

[26] Quinn, J. J.; Chang, H. Y. Unique features of long non-coding RNA biogenesis and function. *Nat. Rev. Genet.* **2016**, *17*, 47–62.

[27] Ørom, U. A.; Derrien, T.; Beringer, M.; Gumireddy, K.; Gardini, A.; Bussotti, G.; Lai, F.; Zytnicki, M.; Notredame, C.; Huang, Q. H. et al. Long noncoding RNAs with enhancer-like function in human cells. *Cell* **2010**, *143*, 46–58.

[28] Fatica, A.; Bozzoni, I. Long non-coding RNAs: New players in cell differentiation and development. *Nat. Rev. Genet.* **2014**, *15*, 7–21.

[29] Lee, J. T. Epigenetic regulation by long noncoding RNAs. *Science* **2012**, *338*, 1435–1439.

[30] Chen, B.; Li, Y.; Zhang, X. Q.; Liu, F.; Liu, Y. L.; Ji, M.; Xiong, F.; Gu, N. An efficient synthesis of ferumoxytol induced by alternating-current magnetic field. *Mater. Lett.* **2016**, *170*, 93–96.

[31] Ma, M.; Zhang, Y.; Shen, X. L.; Xie, J.; Li, Y.; Gu, N. Targeted inductive heating of nanomagnets by a combination of alternating current (AC) and static magnetic fields. *Nano Res.* **2015**, *8*, 600–610.

[32] Lin, X. B.; Gu, N. Surface properties of encapsulating hydrophobic nanoparticles regulate the main phase transition temperature of lipid bilayers: A simulation study. *Nano Res.* **2014**, *7*, 1195–1204.

[33] Tian, F.; Chen, G. C.; Yi, P. W.; Zhang, J. C.; Li, A. G.; Zhang, J.; Zheng, L. R.; Deng, Z.W.; Shi, Q.; Peng, R. et al. Fates of Fe_3O_4 and Fe_3O_4@SiO_2 nanoparticles in human mesenchymal stem cells assessed by synchrotron radiation-based techniques. *Biomaterials* **2014**, *35*, 6412–6421.

[34] Sun, M.; Zhang, G.; Liu, H. J.; Liu, Y.; Li, J. H. α- and γ-Fe_2O_3 nanoparticle/nitrogen doped carbon nanotube catalysts for high-performance oxygen reduction reaction. *Sci. China Mater.* **2015**, *58*, 683–692.

[35] Ashburner, M.; Ball, C. A.; Blake, J. A.; Botstein, D.; Butler, H.; Cherry, J. M.; Davis, A. P.; Dolinski, K.; Dwight, S. S.; Eppig, J. T. et al. Gene ontology: Tool for the unification of biology. *Nat. Genet.* **2000**, *25*, 25–29.

[36] Huang da, W.; Sherman, B. T.; Lempicki, R. A. Systematic and integrative analysis of large gene lists using DAVID bioinformatics resources. *Nat. Protoc.* **2009**, *4*, 44–57.

[37] Kanchanawong, P.; Shtengel, G.; Pasapera, A. M.; Ramko, E. B.; Davidson, M. W.; Hess, H. F.; Waterman, C. M. Nanoscale architecture of integrin-based cell adhesions. *Nature* **2010**, *468*, 580–584.

[38] Jaiswal, R. K.; Jaiswal, N.; Bruder, S. P.; Mbalaviele, G.; Marshak, D. R.; Pittenger, M. F. Adult human mesenchymal stem cell differentiation to the osteogenic or adipogenic lineage is regulated by mitogen-activated protein kinase. *J. Biol. Chem.* **2000**, *275*, 9645–9652.

[39] Zahanich, I.; Graf, E. M.; Heubach, J. F.; Hempel, U.; Boxberger, S.; Ravens, U. Molecular and functional expression of voltage-operated calcium channels during osteogenic differentiation of human mesenchymal stem cells. *J. Bone. Miner. Res.* **2005**, *20*, 1637–1646.

[40] Ge, C. X.; Xiao, G. Z.; Jiang, D.; Franceschi, R. T. Critical role of the extracellular signal-regulated kinase-MAPK pathway in osteoblast differentiation and skeletal development. *J. Cell. Biol.* **2007**, *176*, 709–718.

[41] Bikle, D. D.; Tahimic, C.; Chang, W. H.; Wang, Y. M.; Philippou, A.; Barton, E. R. Role of IGF-I signaling in muscle bone interactions. *Bone* **2015**, *80*, 79–88.

[42] Marie, P. J.; Lomri, A.; Sabbagh, A.; Basle, M. Culture and behavior of osteoblastic cells isolated from normal trabecular bone surfaces. *In Vitro Cell. Dev. Biol.* **1989**, *25*, 373–380.

[43] Pockwinse, S. M.; Wilming, L. G.; Conlon, D. M.; Stein, G. S.; Lian, J. B. Expression of cell growth and bone specific genes at single cell resolution during development of bone tissue-like organization in primary osteoblast cultures. *J. Cell. Biochem.* **1992**, *49*, 310–323.

[44] Bae, J. S.; Gutierrez, S.; Narla, R.; Pratap, J.; Devados, R.; van Wijnen, A. J.; Stein, J. L.; Stein, G. S.; Lian, J. B.; Javed, A. Reconstitution of Runx2/Cbfa1-null cells identifies a requirement for BMP2 signaling through a Runx2 functional domain during osteoblast differentiation. *J. Cell. Biochem.* **2007**, *100*, 434–449.

[45] Wu, M. R.; Chen, G. Q.; Li, Y.-P. TGF-β and BMP signaling in osteoblast, skeletal development, and bone formation, homeostasis and disease. *Bone Res.* **2016**, *4*, 16009.

[46] Nikukar, H.; Reid, S.; Tsimbouri, P. M.; Riehle, M. O.; Curtis, A. S. G.; Dalby, M. J. Osteogenesis of mesenchymal stem cells by nanoscale mechanotransduction. *ACS Nano* **2013**, *7*, 2758–2767.

[47] Yi, C. Q.; Liu, D. D.; Fong, C. C.; Zhang, J. C.; Yang, M. S. Gold nanoparticles promote osteogenic differentiation of mesenchymal stem cells through p38 MAPK pathway. *ACS Nano* **2010**, *4*, 6439–6448.

[48] Young, M. F.; Kerr, J. M.; Ibaraki, K.; Heegaard, A. M.; Robey, P. G. Structure, expression, and regulation of the major noncollagenous matrix proteins of bone. *Clin. Orthop. Relat. Res.* **1992**, 275–294.

[49] Robey, P. G.; Fedarko, N. S.; Hefferan, T. E.; Bianco, P.; Vetter, U. K.; Grzesik, W.; Friedenstein, A.; Van der Pluijm, G.; Mintz, K. P.; Young, M. F. et al. Structure and molecular regulation of bone matrix proteins. *J. Bone Miner. Res.* **1993**, *8*, S483–487.

[50] Komori, T.; Yagi, H.; Nomura, S.; Yamaguchi, A.; Sasaki, K.; Deguchi, K.; Shimizu, Y.; Bronson, R. T.; Gao, Y. H.; Inada, M.et al. Targeted disruption of *Cbfa1* results in a complete lack of bone formation owing to maturational arrest of osteoblasts. *Cell* **1997**, *89*, 755–764.

[51] Otto, F.; Thornell, A. P.; Crompton, T.; Denzel, A.; Gilmour, K. C.; Rosewell, I. R.; Stamp, G. W. H.; Beddington, R. S. P.; Mundlos, S.; Olsen, B. R. et al. *Cbfa1*, a candidate gene for cleidocranial dysplasia syndrome, is essential for osteoblast differentiation and bone development. *Cell* **1997**, *89*, 765–771.

[52] Postigo, A. A. Opposing functions of ZEB proteins in the regulation of the TGFbeta/BMP signaling pathway. *EMBO J.* **2003**, *22*, 2443–2452.

[53] van Grunsven, L. A.; Schellens, A.; Huylebroeck, D.; Verschueren, K. SIP1 (Smad interacting protein 1) and deltaEF1 (delta-crystallin enhancer binding factor) are structurally similar transcriptional repressors. *J. Bone Joint Surg. Am.* **2001**, *83-A*, S40–S47.

[54] Verschueren, K.; Remacle, J. E.; Collart, C.; Kraft, H.; Baker, B. S.; Tylzanowski, P.; Nelles, L.; Wuytens, G.; Su, M. T.; Bodmer, R. et al. SIP1, a novel zinc finger/homeodomain repressor, interacts with Smad proteins and binds to 5'-CACCT sequences in candidate target genes. *J. Biol. Chem.* **1999**, *274*, 20489–20498.

[55] Postigo, A. A.; Depp, J. L.; Taylor, J. J.; Kroll, K. L. Regulation of Smad signaling through a differential recruitment of coactivators and corepressors by ZEB proteins. *EMBO J.* **2003**, *22*, 2453–2462.

[56] Kirschvink, J. L.; Walker, M. M.; Diebel, C. E. Magnetite-based magnetoreception. *Curr. Opin. Neurobiol.* **2001**, *11*, 462–467.

[57] Winklhofer, M.; Kirschvink, J. L. A quantitative assessment of torque-transducer models for magnetoreception. *J. R. Soc. Interface* **2010**, *7*, S273–S289.

[58] Stanley, S. A.; Sauer, J.; Kane, R. S.; Dordick, J. S.; Friedman, J. M. Remote regulation of glucose homeostasis in mice using genetically encoded nanoparticles. *Nat. Med.* **2015**, *21*, 92–98.

[59] Guilak, F.; Cohen, D. M.; Estes, B. T.; Gimble, J. M.; Liedtke, W.; Chen, C. S. Control of stem cell fate by physical interactions with the extracellular matrix. *Cell Stem Cell* **2009**, *5*, 17–26.

[60] Wang, N.; Tytell, J. D.; Ingber, D. E. Mechanotransduction at a distance: Mechanically coupling the extracellular matrix with the nucleus. *Nat. Rev. Mol. Cell Biol.* **2009**, *10*, 75–82.

[61] Mahmoudi, M.; Laurent, S.; Shokrgozar, M. A.; Hosseinkhani, M. Toxicity evaluations of superparamagnetic iron oxide nanoparticles: Cell "vision" versus physicochemical properties of nanoparticles. *ACS Nano* **2011**, *5*, 7263–7276.